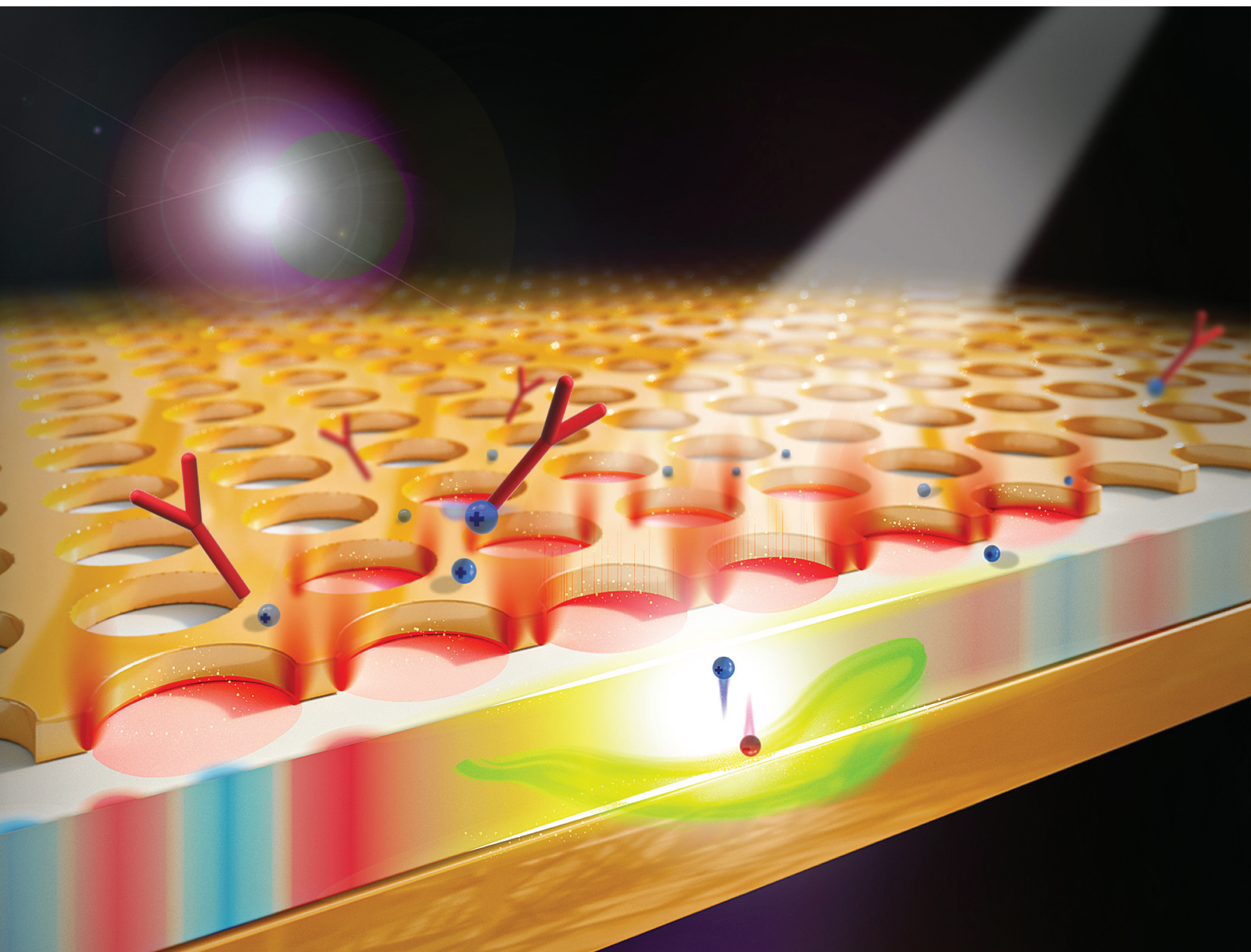


# Nanoscale

rsc.li/nanoscale



ISSN 2040-3372

**COMMUNICATION**

Dangyuan Lei, Xuming Zhang *et al.*  
Enhancing plasmonic hot-carrier generation by strong  
coupling of multiple resonant modes

Cite this: *Nanoscale*, 2021, **13**, 2792Received 25th October 2020,  
Accepted 24th December 2020

DOI: 10.1039/d0nr07643k

rsc.li/nanoscale

## Enhancing plasmonic hot-carrier generation by strong coupling of multiple resonant modes†

Yat Lam Wong,<sup>a</sup> Huaping Jia,<sup>a,b</sup> Aoqun Jian,<sup>b</sup> Dangyuan Lei,<sup>id</sup> \*<sup>c</sup> Abdel I. El Abed<sup>d</sup>  
and Xuming Zhang<sup>id</sup> \*<sup>a</sup>

**Plasmon-induced hot carriers have recently attracted considerable interest, but the energy efficiency in visible light is often low due to the short lifetime of hot carriers and the limited optical absorption of plasmonic architectures. To increase the generation of hot carriers, we propose to exert multiple plasmonic resonant modes and their strong coupling using a metal–dielectric–metal (MDM) nanocavity that comprises an Au nanohole array (AuNHA), a TiO<sub>2</sub> thin film and an Au reflector. Unlike common MDM structures, in addition to the Fabry–Pérot mode in the dielectric layer, AuNHA as the top layer is special because it excites the localized surface plasmon resonance (LSPR) mode in the Au nanoholes and launches the gap surface plasmon polariton (GSPP) mode in the Au reflector surface. The spatial field overlapping of the three resonance modes enables strong mode coupling by optimizing the TiO<sub>2</sub> thickness, which leads to notably enhanced average IPCE (~1.5%) and broadband photocurrent (170  $\mu\text{A}\cdot\text{cm}^{-2}$ ). This MDM structure would be useful for photochemistry and photovoltaics using sunlight.**

## Introduction

Surface plasmon resonance (SPR) excited on metal nanostructures can drastically enhance the interaction of light with matter.<sup>1</sup> Recently, an array of nanoholes perforated on an ultrathin metallic film has demonstrated intriguing plasmonic

properties compared to its complementary counterpart – array of nanoparticles.<sup>2–4</sup> A prominent feature of the plasmonic nanohole array (NHA) is structural continuity, which enables the excitation of surface plasmon polariton (SPP) at two interfaces of the metal film and facilitates the direct electrical connection of the photocurrent. In case the plasmonic film is in the ultrathin regime, the SPP mode on two interfaces would couple together to form a lossy short-range SPP mode, which is prone to the nonradiative dissipation of energy in the film.<sup>5,6</sup> Nevertheless, for an ultrathin plasmonic NHA, the magnitude and broadness of the absorption are limited. Effort has been made to maximize the absorption by integrating plasmonic structures into the conventional metal–dielectric–metal (MDM) structure, which exhibits multiband absorption from the LSPR and the cavity mode.<sup>7–9</sup> In the system with multiple resonances, modes with the same energy in their uncoupled states are often detuned and hybridized into new repulsive states.<sup>10,11</sup> The magnitude of detuning is a direct indication of the strength of the mutual interaction of resonance modes. This concept is vital to harness the spontaneous emission of an emitter for studying cavity quantum electrodynamics.<sup>12,13</sup> In addition to optical absorption, we are interested in the hot carrier generation as a result of plasmonic absorption. Energy acquired from optical absorption can transfer to excitation of an electron–hole pair through Landau damping.<sup>14</sup> The generated carriers are generally referred as “hot” carriers due to the extended tail of Fermi distribution to a higher energy as if the system behaves at a higher effective temperature.<sup>14</sup> Unfortunately, the lifetime of hot carriers is usually in the order of tens of femtoseconds before they undergo relaxation through electron–electron scattering, and therefore a proper strategy for charge separation is crucial to prolong the carriers’ lifetime.<sup>15</sup> Considerable efforts have been made to engineer the hot carrier generation by the rectification effect of the metal–dielectric junction.<sup>16</sup> Recently, the coupling effect between resonance modes have been reported to strongly alter the hot carrier generation associated with plasmon resonance.<sup>17–19</sup> However, only few studies have dis-

<sup>a</sup>Department of Applied Physics, The Hong Kong Polytechnic University, Hong Kong, P.R. China. E-mail: apzhang@polyu.edu.hk

<sup>b</sup>MircoNano System Research Centre, College of Information and Computer Science, Taiyuan University of Technology, Taiyuan, Shanxi 0303024, P.R. China

<sup>c</sup>Department of Materials Science and Engineering, City University of Hong Kong, Hong Kong, P.R. China. E-mail: dangylei@cityu.edu.hk

<sup>d</sup>Laboratoire Lumière Matière et Interfaces (LuMIn), Institut d’Alember, Ecole Normale Supérieure Paris Saclay, CentraleSupélec, CNRS, Université Paris-Saclay, 61 avenue du Président Wilson, 94235 Cachan, France

†Electronic supplementary information (ESI) available: SEM image, AFM, reflection spectra, absorption spectra, GSPP mode, scattering cross-section spectra, IPCE spectra, local electric field spectra. See DOI: 10.1039/d0nr07643k



cussed the influence of the mode coupling effects in the structure on the plasmon-induced hot carrier generation.<sup>17–19</sup> These studies have demonstrated an enhancement of a plasmonic hot carrier generation in the strong coupling regime. The underlying mechanism of the enhancement is suggested to be the modulation of radiative damping resulted from the coherent energy exchange within strongly interacted resonators.<sup>19</sup> Nevertheless, two of these studies only explore the mode coupling effects between plasmonic particles and cavity in the particle/dielectric/metal reflector system.<sup>17,18</sup> The plasmonic hot carrier generation in more complex coupling systems has yet to be carefully examined.

MDM architectures patterned with metallic grating enable SPP modes on the metal–dielectric interface due to the compensation of the momentum mismatch by the ordered nature of the structures.<sup>11</sup> If the metallic grating in the MDM structure supports SPP modes, the SPPs on both metal–dielectric interfaces can couple together to form a guided mode within the dielectric layer, namely, the gap-SPP (GSPP) mode.<sup>20</sup> The symmetric coupling of two SPPs in a nearly lossless dielectric medium results in a high confinement of energy, which we consider to be essential in plasmonic hot carrier generation. However, studies that particularly focus on this issue are yet to be performed.

Herein, we propose a plasmonic absorber with the MDM structure of AuNHA/TiO<sub>2</sub>/Au, which comprises an ultrathin Au nanohole array (AuNHA), a TiO<sub>2</sub> layer and an Au reflector (from top to bottom, Fig. 1a). Three absorption bands that correspond to the cavity mode, the gap-SPP (GSPP) mode, and the LSPR mode appear over the visible to near infrared range. We will demonstrate the evolution of these modes and the

associated plasmon-induced hot carrier generation with respect to the variation of the thickness of TiO<sub>2</sub> layer. The hot carrier generation will be measured by an electrochemical system using the redox couples of Fe<sup>2+</sup>/Fe<sup>3+</sup>.

## Results and discussion

### Morphological characterization

In this work, the AuNHA films are fabricated using nanosphere lithography (NSL) and reactive ion etching (RIE) (more details in the Experimental section). Morphological analysis of the AuNHA is performed by scanning electron microscopy (SEM) and atomic force microscopy (AFM). As one can see from the microscopic images, the nanoholes are arranged in a hexagonal lattice with the periodicity strictly followed the diameter of the unetched polystyrene spheres (see Fig. 1b). The interhole distance and hole diameter have the average values of 265 nm and 222 nm, respectively, as measured from the SEM and histogram in Fig. S1† Based on the three-dimensional contour diagram and the profiles of AFM images (see Fig. S2†), the period and thickness of AuNHA are measured to be 260 nm and 32 nm, respectively.

### Optical characterization

To investigate the influence of TiO<sub>2</sub> thickness on optical properties, AuNHA/TiO<sub>2</sub>/Au MDM absorbers with five different thicknesses of TiO<sub>2</sub> film are numerically and experimentally studied with the focus on their optical absorption spectra. In the simulated spectra (Fig. 2a), three absorption peaks are discernible. For simplicity, the peaks with the shortest, middle, and longest wavelengths are marked as “U”, “M”, and “L”, respectively (representing upper, middle and lower). As the thickness of TiO<sub>2</sub> thin film increases from 30 to 70 nm, the peak “U” presents a red shift and the peak “L” has a blue shift. Interestingly, the peak “M” is insensitive to the variation of TiO<sub>2</sub> thickness. Consequently, the peaks “U” and “L” are squeezed toward the peak “M”; however, they are never merged into one. At the optimal TiO<sub>2</sub> thickness of 55 nm, three peaks are closest. Note that additional increase of TiO<sub>2</sub> thickness does not cause an overlap of resonant peaks. Instead, they repel each other and are shifted to opposite directions. For the absorber with the TiO<sub>2</sub> thickness of 70 nm, the “L” peak becomes weak and broad. In the measured absorption spectra (Fig. 2a), they follow a similar trend with the simulated ones, although the spectral positions of peak “M” deviate from the corresponding simulated values for structures with the TiO<sub>2</sub> thickness of ≥50 nm. The discrepancy can be explained by the energy difference between the simulated and experimental resonant energy of the LSPR mode in the uncoupled state. The uncoupled LSPR mode of AuNHA can be studied by the metal–dielectric (MD) structures that have the AuNHA and TiO<sub>2</sub> film but no back Au reflector (AuNHA/TiO<sub>2</sub>). The calculated spectra show two closely separated peaks; they represent the bonding and anti-bonding LSPR modes of AuNHA (Fig. S3†). In the measured spectra, the resonances are

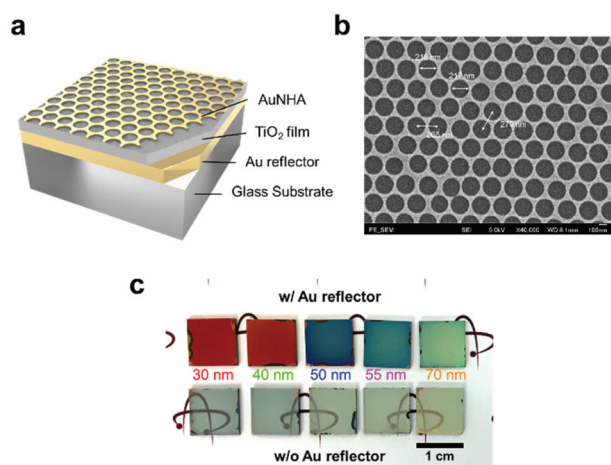


**Fig. 1** (a) Schematic of the AuNHA/TiO<sub>2</sub>/Au metal–dielectric–metal (MDM) absorber proposed in this work; and (b) the scanning electron microscopy (SEM) image of the fabricated Au nanohole array (AuNHA), the hole diameters are 217 and 218 nm and the interhole distances are 265 and 270 nm as marked in the SEM. (c) Images of the fabricated absorbers with (above) and without (below) Au back reflector and having the TiO<sub>2</sub> thicknesses of 30, 40, 50, 55, and 70 nm (from left to right), respectively.

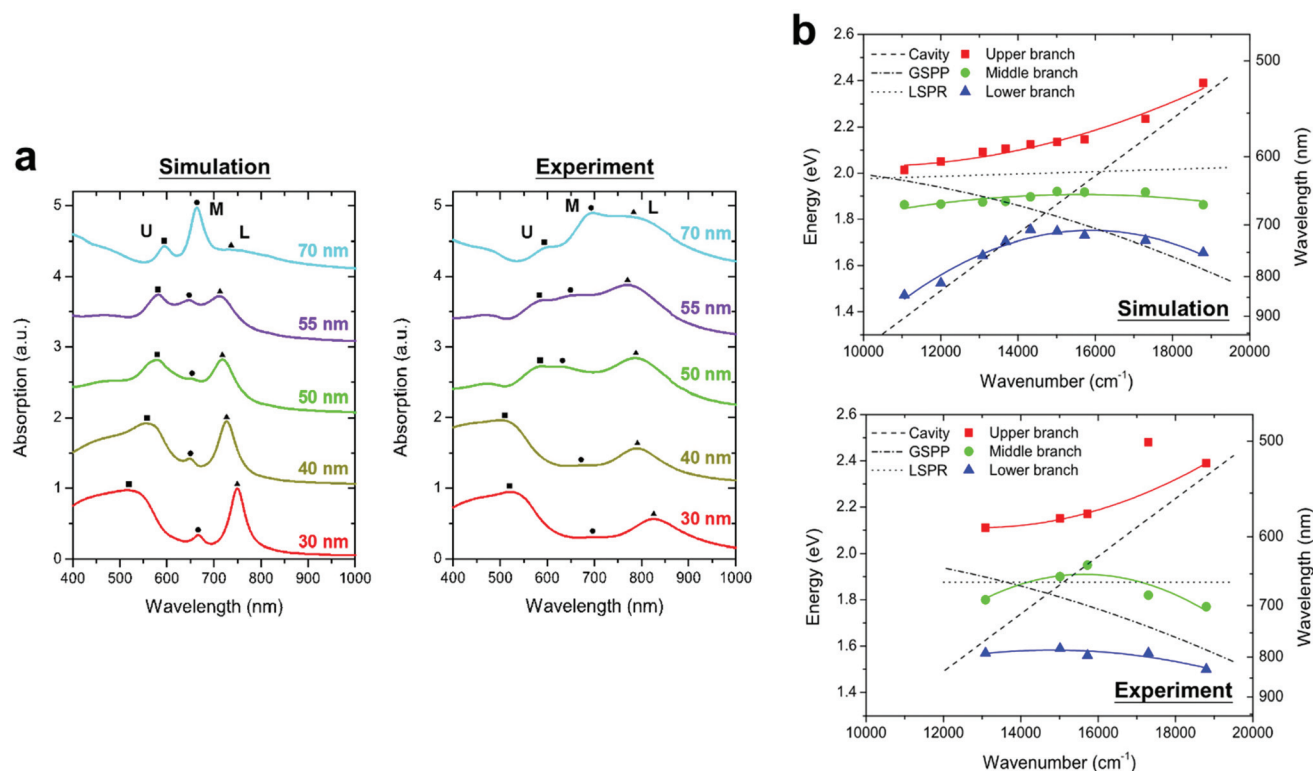


**Fig. 2** (a) FDTD simulated and experimentally measured absorption spectra of the AuNHA/TiO<sub>2</sub>/Au MDM absorbers with the TiO<sub>2</sub> thicknesses of 30, 40, 50, 55, and 70 nm (from bottom to top). The labels “U”, “M”, and “L” represent the upper, middle, and lower branches of resonance, respectively. a.u. stands for arbitrary unit. (b) The FDTD simulated and experimental absorption peak positions of three modes as a function of wavenumber of the cavity mode for the AuNHA/TiO<sub>2</sub>/Au MDM absorbers. The measured absorption peaks are fitted by the parabolic function to show the trends of three branches. For reference, the uncoupled states of the cavity mode, the LSPR mode of Au nanoholes and the GSPP mode are shown as the dashed, dotted, and dash-dotted lines, respectively. The absorber with the TiO<sub>2</sub> thickness of 55 nm is found to fulfil the global strong coupling condition.

broadened and red shifted because of the imperfection of structures fabricated by the NSL technique. Because the experimental uncoupled LSPR energies are considerably closer to the “L” peaks in the coupled system than the simulated spectra, they may have a stronger mode repulsion and lead to a blue-shift of the “M” peak.

Fig. 1c shows the images of the samples of five different TiO<sub>2</sub> thicknesses with or without the Au back reflector. Certain features of the absorption spectra can be seen by the naked eyes from the images. For instance, the structures without the Au back reflector are highly transparent, although the transparency of samples gradually decreases with the increase of TiO<sub>2</sub> thickness. For samples with a back reflector, the color of the samples varies from light red to dark blue, and then to light blue when the TiO<sub>2</sub> thickness increases from 30 to 70 nm. The color change of absorbers with respect to TiO<sub>2</sub> thickness directly correlates to the shift and the hybridization of resonances with respect to TiO<sub>2</sub> thickness illustrated in Fig. 2a.

For analysis, the positions of the absorption peaks of simulated and experimental spectra for MDM absorbers are expressed in eV and plotted against the wavenumber of the cavity mode in Fig. 2b. The wavenumber of cavity mode is esti-

mated from the reflection spectra of the TiO<sub>2</sub>/Au/SiO<sub>2</sub> structure (Fig. S4†). The parabolic fitting curves delineated by resonances can be easily categorized into three branches: upper, middle and lower branches, which never intersect with each other, regardless of the thickness of TiO<sub>2</sub>. The evolution of resonant modes with respect to the change of TiO<sub>2</sub> thickness resembles the characteristics of strongly coupled oscillators.<sup>13</sup>

### Nature of individual modes in the coupled system

For reference, the uncoupled condition of the modes, which corresponds to three absorption peaks in response to the change of cavity resonance wavenumber with varying TiO<sub>2</sub> thickness, are shown in Fig. 2b as the dashed, dash-dotted, and dotted lines to represent the cavity mode, the GSPP mode and the LSPR mode, respectively. They will be discussed one by one as follows.

Regarding the cavity mode (dashed line in Fig. 2b), it is most sensitive to the variation of TiO<sub>2</sub> thickness. To estimate the cavity resonance on its uncoupled condition, we select a bilayer structure with a TiO<sub>2</sub> film and a 100 nm Au film (from upper to lower, TiO<sub>2</sub>/Au in short) and calculate the optical response by the transfer matrix method.<sup>14</sup> The cavity resonance in the TiO<sub>2</sub> film can be read from the reflection dips or

the corresponding maxima in the reflection coefficient spectra (Fig. S4†). Generally, the energy of the cavity resonance is dramatically redshifted with the increase in TiO<sub>2</sub> thickness, and the resonance at large TiO<sub>2</sub> thickness is broad and weak, which matches the trend in the coupled system. The suppression of reflection is primarily contributed by the Fabry-Pérot-like resonance. Two factors cause the cancellation of reflected light, the phase difference due to the imaginary dielectric function of Au and the phase change in the dielectric film.<sup>17,21,22</sup>

Regarding the GSPP mode, it is the only one among the three modes that causes a blue shift of the resonant peak in the MDM absorber (dash-dotted line in Fig. 2b) as it is guided in the dielectric layer sandwiched by two metallic films.<sup>23</sup> The dispersion relation of the GSPP mode for the MDM structure on the uncoupled condition can be calculated using eqn (S1) and (S2).† It is well known that the in-plane wavevector of the SPP mode at the single metal/dielectric interface never matches the wavevector of light at any frequencies; therefore, the SPP mode cannot be excited unless this mismatch is compensated. Similarly, the GSPP mode cannot be directly coupled from the free-space light without the assistance of a grating or the presence of scattering centers.<sup>24,25</sup> Nevertheless, AuNHA in the absorber effectively acts as a grating to provide additional momentum for the excitation of GSPP.<sup>26</sup> The dispersion relation of the GSPP mode for the MDM absorbers with various TiO<sub>2</sub> thicknesses and the momentum provided by grating coupling are plotted in Fig. S5.† As the intersections in the plot represent the resonance energies of GSPP mode enabled by grating coupling, it can be seen from Fig. S5† that the energy of GSPP is blue-shifted with the increase of TiO<sub>2</sub> thickness and this trend is consistent with the trends in both the FDTD and experimental spectra of the coupled system. The formation of GSPP can be depicted by the coupling between the SPP modes propagated at two dielectric/metal interfaces through their evanescent fields.<sup>27</sup> GSPP is similar to the coupled SPP mode supported in an ultrathin AuNHA, although the coupled SPP is usually formed by the anti-symmetrical coupling with a highly lossy characteristic; however, GSPP is formed by the symmetrical coupling with a long propagation length.<sup>20,28</sup> For better understanding of the GSPP mode in the proposed MDM absorber, we conduct the FDTD analysis of the MDM absorber with short-range ordered nanoholes. Through electrodynamic simulations, the propagation of GSPP mode confined within the TiO<sub>2</sub> layer can be clearly visualized in both the frequency and time-domain manners. The detailed discussions are presented in ESI Discussion 1.†

Regarding the LSPR mode, its resonance is supported by the nanoholes of the AuNHA layer (dotted line in Fig. 2b). Here, we assume that the resonance of nanoholes in the MDM structure follows the resonance of an AuNHA on a layer of TiO<sub>2</sub>, as already shown in Fig. S4.† However, this assumption cannot always be appropriate because the coupling effect between AuNHA and its own image induced by the back reflector alters the resonance energy especially when the thickness of TiO<sub>2</sub> is thin.<sup>29–31</sup> To demonstrate the shift of resonance

under the SPR-image coupling effect, we alternatively studied the decoupled SPR using a special MDM system that has a top Au film perforated with only one nanohole (diameter 220 nm), a middle TiO<sub>2</sub> layer and an Au back reflector. Based on the FDTD-simulated scattering spectra of the structure in Fig. S6,† the SPR peak of the single-hole system is gradually redshifted with increase in the TiO<sub>2</sub> thickness. In both cases, the SPR of AuNHA and single nanohole show a relatively stable shift of resonance energy in response to the change of TiO<sub>2</sub> thickness as compared to other two modes. Nevertheless, we decided to use the resonance of an AuNHA on a layer of TiO<sub>2</sub> to interpret the LSPR resonance in the coupled system as the SPR in an ordered lattice is fundamentally different from an isolated structure.<sup>32</sup>

### Strong coupling condition

Anti-crossing behaviour can be observed in Fig. 2b, which indicated the existence of modal strong coupling. The fulfilment of strong coupling condition can be evaluated by the linewidth and the energy splitting of the resonances using the relationship  $\Omega > (\gamma_U + \gamma_L)/2$ , where  $\Omega$  is the energy splitting, while  $\gamma_U$  and  $\gamma_L$  are the linewidths of the upper and lower branch resonances, respectively.<sup>33</sup> In a more complicated system that involves the hybridization of three modes, the criterion can be adapted to a global strong coupling condition as follows:

$$\Omega_{U-L} > \gamma_M > (\gamma_M + \gamma_{U,L})/2 \quad (1)$$

where  $\Omega_{U-L}$  refers to the splitting between the upper and lower branches,  $\gamma_M$  denotes the linewidth of the middle branch, and  $\gamma_{U,L}$  represents either  $\gamma_U$  or  $\gamma_L$ .<sup>34</sup> The global minimum of splitting occurs when the MDM absorber has the TiO<sub>2</sub> thickness of 55 nm (this absorber is named as MDM55 hereafter), which will be used to analyze the strong coupling condition. To obtain the linewidth of resonances, multiple Lorentzian fits are implemented on the simulated and experimented absorption spectra, as illustrated in Fig. S7.† As summarized in Table 1, the experimental spectra give  $\gamma_U = 278$  meV,  $\gamma_M = 509$  meV, and  $\gamma_L = 329$  meV, whereas the simulated spectra yield  $\gamma_U = 217$  meV,  $\gamma_M = 212$  meV, and  $\gamma_L = 182$  meV. The splitting energy  $\Omega_{U-L}$  is directly extracted from the anti-crossing plots to be 560 meV for the experiment and 400 meV for the simulation. Correspondingly, the parameters  $(\gamma_M + \gamma_U)/2$  and  $(\gamma_M + \gamma_L)/2$  are 394 and 419 meV for experiment and 215 and 197 meV for simulation. Substituting all values into eqn (1),

**Table 1** Analysis of strong mode coupling.  $\Omega_{U-L}$  refers to the splitting between the upper and lower branches,  $\gamma_U$ ,  $\gamma_M$ , and  $\gamma_L$  denote the linewidths of the upper branch, the middle branch, and the lower branch, respectively

	$\Omega_{U-L}$	$\gamma_U$	$\gamma_M$	$\gamma_L$	$(\gamma_M + \gamma_U)/2$	$(\gamma_M + \gamma_L)/2$	Strong coupling condition
Experiment	560	278	509	329	394	419	Fulfilled
FDTD	400	217	212	182	215	197	Fulfilled



one can find that the strong coupling criterion is satisfied in both experimental and simulated spectra. Note that the parabolic fitting curves in Fig. 2b merely serve to visualize the trend of each branch but without any physical meaning. Ideally, a coupled harmonic oscillator model should be used to confirm the composition of model coupling in the dispersion diagram.<sup>17,34</sup> Unfortunately, this is unachievable in this system. Due to the inseparable nature between the plasmon resonance of the nanohole array and the GSPP mode in the dielectric layer, the linewidth of the GSPP resonance in the uncoupled state cannot be measured in an unambiguous manner.

### Plasmonic hot carrier generation

To quantify the plasmon-induced hot carrier generation using absorbers, the samples are measured on the photocatalytic efficiency associated with the reduction and oxidation of  $\text{Fe}^{2+}$  and  $\text{Fe}^{3+}$ , respectively.<sup>35,36</sup> The carrier generation and transport in the electrochemical system is illustrated in Fig. 3a. The incident photon-to-current conversion efficiencies (IPCEs) for the absorbers with various  $\text{TiO}_2$  thicknesses are measured using 14 monochromatic light sources (Fig. 3d and Fig. S8†). For easy reference, the experimental absorption spectra of the same absorbers are also plotted. Reasonable agreement can be seen between the IPCE spectra and the absorption spectra in terms of the peak positions and general trends. Note that the  $\text{TiO}_2$  thicknesses of 50 nm and 55 nm produce higher IPCE

(max.  $\sim 1.5\%$ ) compared to other thicknesses. Similar dependence of  $\text{TiO}_2$  thickness is observed in the measured photocurrent of absorbers under the irradiation of broadband visible light ( $\lambda > 490$  nm). As can be seen from Fig. 3b and c, MDM55 produces the highest photocurrent density (max.  $170 \mu\text{A cm}^{-2}$ ) in the ON state, and MDM30 gives the second highest photocurrent of  $135 \mu\text{A cm}^{-2}$ . Consequently, the MDM structure with strong coupling effect enhances the photocurrent by a factor of at least 1.26 compared to the ones without the strong coupling effect. To prove that the photocurrent generated by the semiconductor itself is small, a bare  $\text{TiO}_2$  film of 70 nm thick (marked as T70 in Fig. 3c) is prepared and tested, a negligible current of only  $0.25 \mu\text{A cm}^{-2}$  is measured from the bare  $\text{TiO}_2$  film as expected. Note that MDM55 enhances the photocurrent by a factor of 680 compared to the bare  $\text{TiO}_2$  film (70 nm thick).

Both IPCE and photocurrent measurement show strong correlation between the plasmonic enhancement and the strong coupling effect of the three resonant modes of the AuNHA/ $\text{TiO}_2$ /Au MDM absorbers. Such an intriguing phenomenon in the strong coupling system was reported by Misawa,<sup>17</sup> however, the detailed interpretation underneath this phenomenon is elusive. Misawa suggested that the coupled SPR mode has a higher tendency to decay into electron-hole pairs (EHPs) as the dephasing time of SPR mode under the strong coupling condition is shorter than that of the regular SPR mode as proved by the time-resolved photoemission electron

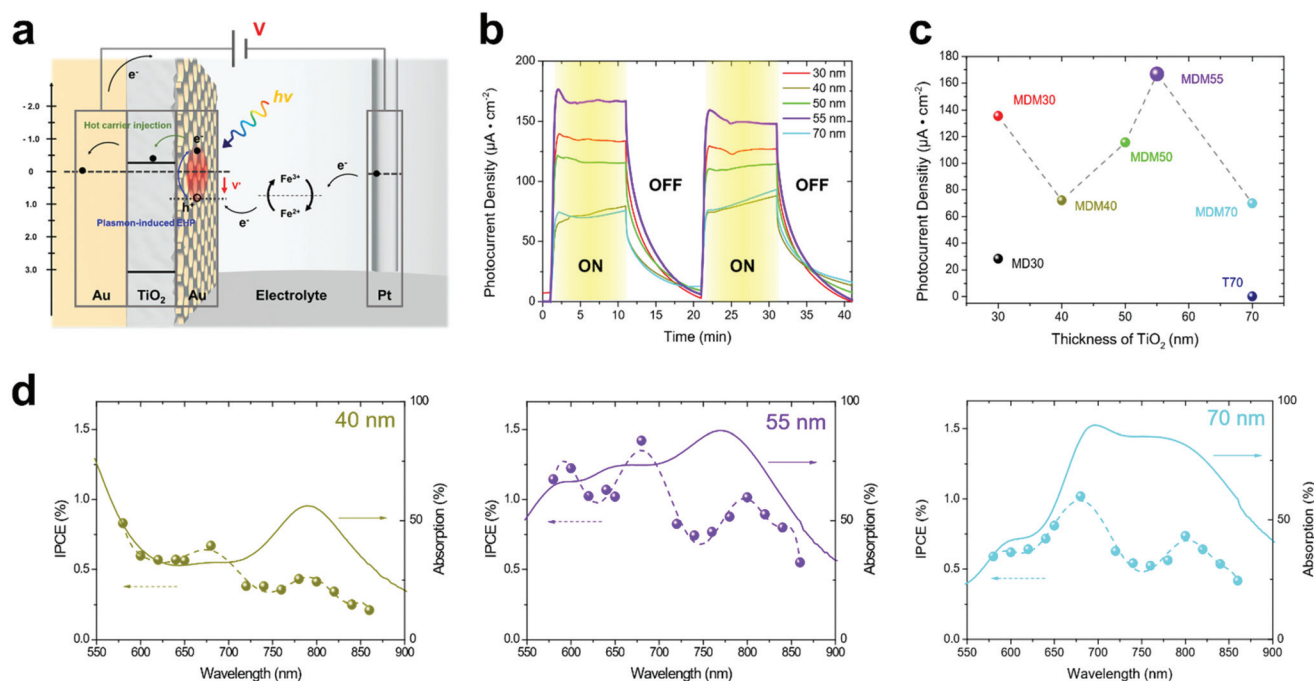


**Fig. 3** (a) The schematic diagram of the hot carrier excitation and transport amid the absorber, the Pt electrode, and the  $\text{Fe}^{2+}/\text{Fe}^{3+}$  redox system. (b) The transient photocurrent density of the AuNHA/ $\text{TiO}_2$ /Au MDM absorbers under the ON/OFF illumination of broadband visible light (wavelength  $> 490$  nm). (c) The stable photocurrent density of the absorbers as a function of the  $\text{TiO}_2$  thickness. T70 represents the structure of bare  $\text{TiO}_2$  film with the thickness of 70 nm. (d) The IPCE spectra (left axis) and the absorption spectra (right axis) of the MDM structures with the optimized  $\text{TiO}_2$  thickness (55 nm) and with unoptimized  $\text{TiO}_2$  thicknesses (40 and 70 nm). All the photocurrents and IPCEs are measured under the bias voltage of 0.5 V vs. SCE.

microscopy.<sup>11,17,19</sup> The proposed interpretation of the enhancement mechanism is as follows. Under the strong coupling condition (*i.e.* MDM55), energy of the three resonant modes is able to exchange coherently. As the excitation of GSPP relies on the coupling between the LSPR of AuNHA and the guiding mode in the dielectric layer, coherent energy exchange leads to a preminent channel for energy confinement or otherwise radiatively decaying into free space for the system in a weak coupling regime.<sup>19</sup> The confinement of energy through GSPP mode not only can effectively prolong the plasmon lifetime, but also can increase the generation of plasmonic hot carriers since the SPP is intrinsically prone to decaying non-radiatively.<sup>19</sup> The cavity resonance plays an important role in maintaining high optical field in the dielectric layer to further facilitate the excitation of LSPR on AuNHA and its coupling with the GSPP mode.

Here, we find that the average optical absorption over the visible and near infrared range reaches a maximum when the MDM absorber has the TiO<sub>2</sub> thickness of 55 nm (Fig. S9†). This further implies that the generation of hot carrier is primarily caused by the plasmonic absorption. To top this, the intense local field plays another important role in the enhancement of photocatalytic efficiency. Numerous prior studies have already proved that the plasmon-induced hot carrier generation is an electric-field driven event in which the rate of generation is proportional to the local field enhancement of SPR.<sup>37–40</sup> To verify the correlation between the strong coupling condition and the local electric field enhancement, the local field intensity in the absorbers is probed by surface-enhanced Raman spectroscopy (SERS).<sup>41</sup> The Raman signal intensity is known to be proportional to the fourth power of the local electric field enhancement, namely  $I_{\text{Raman}} \propto (E_{\text{loc}}/E_0)^4$ .<sup>4</sup> Since the TiO<sub>2</sub> material possesses sharp Raman peaks<sup>42</sup> and the TiO<sub>2</sub> film is sandwiched between two metallic structures in the AuNHA/TiO<sub>2</sub>/Au MDM structures, these make the SERS signal a suitable indicator of the local field in structures.<sup>41</sup> The SERS measurements record the strongest enhancement of Raman signals of TiO<sub>2</sub> from MDM55 than all other structures (Fig. 4). To verify whether

the SERS of the absorber is contributed by the local field enhancement, we particularly use the FDTD simulation to investigate the electric field enhancement spectra at the middle point of the TiO<sub>2</sub> layer of the absorbers (under three conditions, one strong MDM55 and two weak coupling conditions MDM30 and MDM70) and the absorber without the back reflector (*i.e.*, MD30 (Fig. S10†). One can see that MDM55 presents the largest field enhancement near the excitation laser wavelength (the dashed line in the left panel of Fig. S10†), and the trend of electric field enhancements of the absorbers follows that of the SERS results. Note that the field confinement in our proposed system behaves quite differently from ordinary particle-on-film system in which the field enhancement is maximized by minimizing the thickness of the dielectric (usually within a few nanometers).<sup>30</sup> In Fig. S10,† the absorber with the thinnest TiO<sub>2</sub> thickness (*i.e.* MDM30) has a weak electric field enhancement compared to the absorber with a thick TiO<sub>2</sub> (*i.e.* MDM55 or MDM70), which indicates that the field enhancement depends on the coupling condition that is sensitive to the TiO<sub>2</sub> thickness as already discussed. Since the evanescent field of the LSPR on the AuNHA needs to be extended by a fairly long distance (>30 nm) to interact with the lower film, the field intensity would be significant only if the coupling strength is strong, especially for the GSPP and cavity mode. For MDM55, the detuning is small and yet the strong coupling condition is satisfied, the energies of the three resonant mode (*i.e.*, the cavity, the GSPP and the SPR) can reversibly exchange, which leads to an enhancement of the weak evanescent field in the dielectric layer compared to the other case with a large detuning or a weak coupling system.<sup>11</sup> Fig. S11† shows the internal quantum efficiency (IQE) of the MDM absorber with a strong coupling effect, the MDM absorber without a strong coupling effect (*i.e.*, with weak coupling effect) and the MD absorber (without reflector). The carrier generated from the absorber with the strong mode coupling effect manifests an elevated IQE compared to the structure with weak coupling effect and the one with mono-plasmon mode (without reflector). This, once again, further demonstrates that the enhancements in IPCE found in the MDM system are attributed to the prolonged carrier's lifetime and the near-field enhancement as a consequence of mode coupling effect rather than merely the enhanced optical absorption, as the IQE is normalized to the number of absorbed photons.<sup>43</sup> Therefore, the superior performance of the hot carrier generation in MDM55 can be attributed to the intense local electric field generated by the interplay of three modes under the strong coupling condition.<sup>44,45</sup>

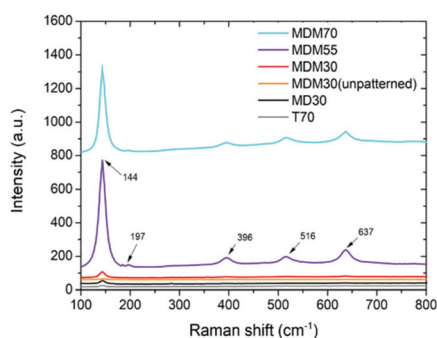


**Fig. 4** The measured Raman spectra of the AuNHA/TiO<sub>2</sub>/Au MDM absorbers with different TiO<sub>2</sub> thicknesses. MD30 represents the absorbers without the back Au reflector, and T70 denotes the absorber with only a bare TiO<sub>2</sub> layer. They are used as controls.

## Conclusion

This work has studied the relationship between the mode coupling effect of the AuNHA/TiO<sub>2</sub>/Au MDM structure and the plasmon-induced hot carrier generation *via* an electrochemical system. With the change of TiO<sub>2</sub> thickness in the MDM absor-

ber, the three resonant modes present an anti-crossing behaviour and satisfy the strong coupling condition. For the MDM structures with different  $\text{TiO}_2$  thicknesses, the IPCE spectra follow the general trend of the absorption spectra. The optimal MDM absorber with the 55 nm-sized  $\text{TiO}_2$  layer produces the maximum IPCE of 1.5% and yields an enhanced photocurrent (enhanced by at least 1.26 times) as a result of the plasmon-induced hot carrier generation. The enhancement is attributed to the strong local field confined within the cavity by the mode hybridization as confirmed by both the SERS measurements and the FDTD simulations. This work presents a highly-efficient plasmonic absorber design, which may find potential applications in visible-light photocatalysis.

## Experimental section

### Sample fabrication

Prior to film deposition, the fluorine-doped tin oxide (FTO) glasses are pre-cleaned sequentially by ultrasonically in acetone, isopropanol, and DI water for 10 min each. They are then dried by pure nitrogen and treated by oxygen plasma (Harrick) to remove any residual organic substances on substrates. The gold back reflector is deposited onto the FTO glasses by magnetron sputtering deposition (Denton). Before deposition, the chamber is evacuated by a cryopump until the base pressure reached below  $9 \times 10^{-7}$  Torr. Gold with purity of 99.99% is used as a target. During deposition, sputtering power of 80 W and argon flow of 30 sccm is maintained.  $\text{TiO}_2$  film is deposited onto the gold reflectors or the FTO substrates by atomic layer deposition (ALD) (Ultratech). Chemical precursor with Ti and  $\text{H}_2\text{O}$  are alternately introduced into the chamber in each cycle. The ALD process is implemented at 150 °C and the deposition rate is reported to be 0.47 Å per cycle. After deposition, the samples with  $\text{TiO}_2$  thin film are then annealed in air for 1 h at 400 °C to transform  $\text{TiO}_2$  from amorphous to anatase phase. A Au nanohole array is fabricated by NSL and RIE process. The polystyrene nanosphere with 10% solid suspended in DI water is purchased from the market. The suspension is then diluted with 1:1 v% absolute ethanol and dispersed by ultrasonically every time before use. The detailed procedure of NSL can be reported in other studies.<sup>46,47</sup> In brief, 20 µl polystyrene nanosphere suspension is dropwise added onto the water surface of a reservoir. Subsequently, few drops of sodium dodecyl sulfate (SDS) are added to reduce the surface tension of water. To obtain high-quality closely packed nanosphere template, the hydrophilicity of the substrate is crucial. Thus, the as-deposited  $\text{TiO}_2$  films are treated by oxygen plasma (Harrick) for 2 min to increase the hydrophilicity of the surface. The closely packed nanospheres are carefully transferred from the water surface onto the as-deposited  $\text{TiO}_2$  films and are then left to naturally dry. To fabricate the evaporation mask for nanohole array, the closely packed nanospheres on  $\text{TiO}_2$  film are isotropically etched by Oxygen RIE

technique (Trion). During etching, the flow of purging  $\text{O}_2$ , working pressure, and RIE power are set at 30 sccm, 250 mTorr and 80 W, respectively. The etching rate is about  $1.2 \text{ nm s}^{-1}$  confirmed by SEM images. The resultant etched nanospheres are then used as the evaporation mask to fabricate AuNHAs by the electron beam evaporation (Denton). Gold pellets with purity of 99.99% are used as an evaporation source. The evaporation is conducted until the base pressure of the chamber is reached below  $9 \times 10^{-7}$  Torr. During deposition, the substrate holder is rotated at a constant rate of 20 rpm to ensure film uniformity. The deposition rate and thickness are controlled by a quartz crystal monitor (INFICON). The deposition rate is maintained at  $0.5 \text{ Å s}^{-1}$  to retain good adhesion, good control of thickness and low roughness. The AuNHA pattern is finally obtained after the lift-off of the nanosphere template by an ultrasonic bath in toluene.

### Characterization

The morphology of nanostructures is studied by images acquired by the field-emission scanning electron microscope (FESEM) (JEOL). The reflection spectra of samples are measured by the UV-visible spectrometer coupled with an integrating sphere (PerkinElmer). Both the scattering and specular reflection signal are recorded inside the integrating sphere for non-transparent samples in a single measurement. Therefore, the absorption spectrum  $A$  can be calculated as  $A(\lambda) = 1 - R(\lambda)$ , where  $R$  represents the reflection spectrum.

### Numerical simulation

The theoretical calculation of far-field and near-field spectra is performed by Finite-Difference Time-Domain (FDTD) software (Lumerical). To simulate the structures with a nanohole array, a unit cell with the periodic boundaries in the  $x$ - and  $y$ -directions is implemented. A plane-wave source is injected from the air side to the structure. For simulations involving the time-averaging or wavelength dependent spectra, Fourier transform monitors are employed. Since the scattered light can be fully recorded by a 2D monitor, the absorption,  $A$ , of structures is generally defined as  $A(\lambda) = 1 - R(\lambda) - T(\lambda)$ , where  $R$  is the reflection and  $T$  is the transmission. Override mesh with the size of 0.8 nm is established near the nano-patterns and convergence testing is conducted to ensure the precision of simulation. The dielectric functions of Au,  $\text{SiO}_2$ , and  $\text{TiO}_2$  used for simulation are adopted from previous studies.<sup>48–50</sup>

### Photoelectrochemical measurements

The photocurrent is measured by the three-electrode configuration electrochemical cell. The testing samples, platinum wire, and saturated calomel electrode (SCE) are used as the working electrode, counter electrode, and reference electrode, respectively. Three electrodes are connected to an electrochemical station for characterization. The electrolyte solution used in this work contains 2.5 mM  $\text{Fe}_2(\text{SO}_4)_3$ , 10 mM  $\text{FeSO}_4$ , and 0.5 M  $\text{Na}_2\text{SO}_4$ . For the measurement of current generation by the broadband light, a Xe light source of 150 W equipped with a



490 nm long-pass filter is used. In the IPCE measurement, band pass filters are coupled with the 150 W xenon light source. The IPCE is calculated by

$$\text{IPCE}(\lambda) = \frac{1240 \cdot I(\text{A cm}^{-2})}{\lambda(\text{nm}) \cdot P(\text{W cm}^{-2})}$$

where  $I$  and  $P$  are the photocurrent density and the optical power of the source, respectively. The optical power of monochromatic light is measured by a handheld power meter (ThorLab). All photocurrent signals in this work are measured under the bias of 0.5 V vs. SCE.

### Raman spectra measurements

All Raman spectra are measured by a commercial confocal Raman spectrometer (alpha300, WITec). Two laser sources of wavelength (532 nm and 633 nm), a monochromator, and a Peltier cooled CCD unit are integrated into a single spectrometer. All spectra are measured as a function of Raman shift. The characterization of samples with  $\text{TiO}_2$  is performed by the laser source with the wavelength of 633 nm, optical power of 1 mW and in the spectral range of 100–900  $\text{cm}^{-1}$ .

### Conflicts of interest

There are no conflicts to declare.

### Acknowledgements

This work is supported by the Research Grants Council of Hong Kong (152184/15E, 152127/17E, 152126/18E, 152219/19E, 152156/20E, 15304519 and N\_PolyU511/20), The Hong Kong Polytechnic University (1-ZE14, 1-ZE27 and 1-ZVGH), The City University of Hong Kong (9610434). The technical assistance and facility support from Materials Research Centre and from the University Research Facility in Material Characterization and Device Fabrication of The Hong Kong Polytechnic University are acknowledged.

### References

- 1 M. Pelton and G. W. Bryant, *Introduction to metal-nanoparticle plasmonics*, John Wiley & Sons, 2013.
- 2 B. Ai, Z. Wang, H. Moehwald and G. Zhang, *ACS Nano*, 2017, **11**, 12094–12102.
- 3 J. T. Li, S. K. Cushing, P. Zheng, F. K. Meng, D. Chu and N. Q. Wu, *Nat. Commun.*, 2013, **4**, 2651.
- 4 D. Tordera, D. Zhao, A. V. Volkov, X. Crispin and M. P. Jonsson, *Nano Lett.*, 2017, **17**, 3145–3151.
- 5 J. Braun, B. Gompf, G. Kobiela and M. Dressel, *Phys. Rev. Lett.*, 2009, **103**, 203901.
- 6 M. Liu, Y. Song, Y. Zhang, X. Wang and C. Jin, *Plasmonics*, 2012, **7**, 397–410.
- 7 Q. Li, Z. Li, X. Wang, T. Wang, H. Liu, H. Yang, Y. Gong and J. Gao, *Nanoscale*, 2018, **10**, 19117–19124.
- 8 Q. Li, Z. Z. Li, H. G. Yang, H. Liu, X. Y. Wang, J. S. Gao and J. L. Zhao, *Opt. Express*, 2016, **24**, 25885–25893.
- 9 Q. Shi, T. U. Connell, Q. Xiao, A. S. R. Chesman, W. Cheng, A. Roberts, T. J. Davis and D. E. Gomez, *ACS Photonics*, 2019, **6**, 314–321.
- 10 E. S. H. Kang, S. Chen, S. Sardar, D. Tordera, N. Armakavicius, V. Darakchieva, T. Shegai and M. P. Jonsson, *ACS Photonics*, 2018, **5**, 4046–4055.
- 11 J. H. Yang, Q. Sun, K. Ueno, X. Shi, T. Oshikiri, H. Misawa and Q. H. Gong, *Nat. Commun.*, 2018, **9**, 8.
- 12 S. Savasta, R. Saija, A. Ridolfo, O. Di Stefano, P. Denti and F. Borghese, *ACS Nano*, 2010, **4**, 6369–6376.
- 13 K. Hennessy, A. Badolato, M. Winger, D. Gerace, M. Atature, S. Gulde, S. Falt, E. L. Hu and A. Imamoglu, *Nature*, 2007, **445**, 896–899.
- 14 M. L. Brongersma, N. J. Halas and P. Nordlander, *Nat. Nanotechnol.*, 2015, **10**, 25–34.
- 15 X. Zhang, Y. L. Chen, R.-S. Liu and D. P. Tsai, *Rep. Prog. Phys.*, 2013, **76**, 046401.
- 16 M. W. Knight, H. Sobhani, P. Nordlander and N. J. Halas, *Science*, 2011, **332**, 702–704.
- 17 X. Shi, K. Ueno, T. Oshikiri, Q. Sun, K. Sasaki and H. Misawa, *Nat. Nanotechnol.*, 2018, **13**, 953.
- 18 Y. F. Cao, T. Oshikiri, X. Shi, K. Ueno, J. Li and H. Misawa, *ChemNanoMat*, 2019, **5**, 1008–1014.
- 19 H. Y. Shan, Y. Yu, X. L. Wang, Y. Luo, S. Zu, B. W. Du, T. Y. Han, B. W. Li, Y. Li, J. R. Wu, F. Lin, K. B. Shi, B. K. Tay, Z. Liu, X. Zhu and Z. Y. Fang, *Light: Sci. Appl.*, 2019, **8**, 9.
- 20 J. Jung, T. Sondergaard and S. I. Bozhevolnyi, *Phys. Rev. B*, 2009, **79**, 035401.
- 21 H. Dotan, O. Kfir, E. Sharlin, O. Blank, M. Gross, I. Dumchin, G. Ankonina and A. Rothschild, *Nat. Mater.*, 2013, **12**, 158–164.
- 22 M. A. Kats, R. Blanchard, S. Ramanathan and F. Capasso, *Opt. Photonics News*, 2014, **25**, 40–47.
- 23 S. I. Bozhevolnyi, V. S. Volkov, E. Devaux, J. Y. Laluet and T. W. Ebbesen, *Nature*, 2006, **440**, 508–511.
- 24 S. A. Maier, *Plasmonics: fundamentals and applications*, Springer Science & Business Media, 2007.
- 25 E. J. C. Dias and F. J. G. de Abajo, *ACS Nano*, 2019, **13**, 5184–5197.
- 26 C. Genet and T. W. Ebbesen, *Nature*, 2007, **445**, 39–46.
- 27 J. A. Dionne, L. A. Sweatlock, H. A. Atwater and A. Polman, *Phys. Rev. B*, 2006, **73**, 035407.
- 28 F. Yang, J. Sambles and G. Bradberry, *Phys. Rev. B: Condens. Matter Mater. Phys.*, 1991, **44**, 5855.
- 29 G. C. Li, Y. L. Zhang, J. Jiang, Y. Luo and D. Y. Lei, *ACS Nano*, 2017, **11**, 3067–3080.
- 30 G. C. Li, Q. Zhang, S. A. Maier and D. Lei, *Nanophotonics*, 2018, **7**, 1865–1889.
- 31 A. Sobhani, A. Manjavacas, Y. Cao, M. J. McClain, F. Javier, G. de Abajo, P. Nordlander and N. J. Halas, *Nano Lett.*, 2015, **15**, 6946–6951.

- 32 V. G. Kravets, A. V. Kabashin, W. L. Barnes and A. N. Grigorenko, *Chem. Rev.*, 2018, **118**, 5912–5951.
- 33 G. Khitrova, H. M. Gibbs, M. Kira, S. W. Koch and A. Scherer, *Nat. Phys.*, 2006, **2**, 81–90.
- 34 J. Cuadra, D. G. Baranov, M. Wersall, R. Verre, T. J. Antosiewicz and T. Shegai, *Nano Lett.*, 2018, **18**, 1777–1785.
- 35 N. Sakai, Y. Fujiwara, Y. Takahashi and T. Tatsuma, *ChemPhysChem*, 2009, **10**, 766–769.
- 36 Y. Nishijima, K. Ueno, Y. Yokota, K. Murakoshi and H. Misawa, *J. Phys. Chem. Lett.*, 2010, **1**, 2031–2036.
- 37 K. Saito, I. Tanabe and T. Tatsuma, *J. Phys. Chem. Lett.*, 2016, **7**, 4363–4368.
- 38 E. Kazuma, N. Sakai and T. Tatsuma, *Chem. Commun.*, 2011, **47**, 5777–5779.
- 39 H. Lee, H. Lee and J. Y. Park, *Nano Lett.*, 2019, **19**, 891–896.
- 40 E. Cortes, W. Xie, J. Cambiasso, A. S. Jermyn, R. Sundararaman, P. Narang, S. Schlucker and S. A. Maier, *Nat. Commun.*, 2017, **8**, 14880.
- 41 D. Liu, T. Wu, Q. Zhang, X. Wang, X. Guo, Y. Su, Y. Zhu, M. Shao, H. Chen, Y. Luo and D. Lei, *ACS Nano*, 2019, **13**, 7644–7654.
- 42 W. F. Zhang, Y. L. He, M. S. Zhang, Z. Yin and Q. Chen, *J. Phys. D: Appl. Phys.*, 2000, **33**, 912–916.
- 43 G. Tagliabue, A. S. Jermyn, R. Sundararaman, A. J. Welch, J. S. DuChene, R. Pala, A. R. Davoyan, P. Narang and H. A. Atwater, *Nat. Commun.*, 2018, **9**, 8.
- 44 K. H. W. Ho, A. X. Shang, F. H. Shi, T. W. Lo, P. H. Yeung, Y. S. Yu, X. M. Zhang, K. Y. Wong and D. Y. Lei, *Adv. Funct. Mater.*, 2018, **28**, 1800383.
- 45 D. C. Ratchford, A. D. Dunkelberger, I. Vurgaftman, J. C. Owrutsky and P. E. Pehrsson, *Nano Lett.*, 2017, **17**, 6047–6055.
- 46 P. Gao, J. He, S. Zhou, X. Yang, S. Li, J. Sheng, D. Wang, T. Yu, J. Ye and Y. Cui, *Nano Lett.*, 2015, **15**, 4591–4598.
- 47 H. Li, J. Low, K. S. Brown and N. Wu, *IEEE Sens. J.*, 2008, **8**, 880–884.
- 48 P. B. Johnson and R.-W. Christy, *Phys. Rev. B: Solid State*, 1972, **6**, 4370.
- 49 E. D. Palik, *Handbook of optical constants of solids*, Academic press, 1998.
- 50 M. Hasan, A. Haseeb, R. Saidur and H. H. Masjuki, *Int. J. Chem. Biol. Eng.*, 2008, **1**, 92–96.